

Computing sessile droplet shapes on arbitrary surfaces with a new pairwise-force smoothed particle hydrodynamics model

Riley M. Whebell¹ , Timothy J. Moroney¹, Ian W. Turner¹,
Ravindra Pethiyagoda²  and Scott W. McCue¹ 

¹School of Mathematical Sciences, Queensland University of Technology, Brisbane, QLD 4000, Australia

²School of Information and Physical Sciences, University of Newcastle, Callaghan, NSW 2308, Australia

Corresponding author: Riley M. Whebell, whebell2@qut.edu.au

(Received 29 October 2024; revised 22 June 2025; accepted 11 August 2025)

The study of the shape of droplets on surfaces is an important problem in the physics of fluids and has applications in multiple industries, from agrichemical spraying to microfluidic devices. Motivated by these real-world applications, computational predictions for droplet shapes on complex substrates – rough and chemically heterogeneous surfaces – are desired. Grid-based discretisations in axisymmetric coordinates form the basis of well-established numerical solution methods in this area, but when the problem is not axisymmetric, the shape of the contact line and the distribution of the contact angle around it are unknown. Recently, particle methods, such as pairwise-force smoothed particle hydrodynamics (PF-SPH), have been used to conveniently forego explicit enforcement of the contact angle. The pairwise-force model, however, is far from mature, and there is no consensus in the literature on the choice of pairwise-force profile. We propose a new pair of polynomial force profiles with a simple motivation and validate the PF-SPH model in both static and dynamic tests. We demonstrate its capabilities by computing droplet shapes on a physically structured surface, a surface with a hydrophilic stripe and a virtual wheat leaf with both micro-scale roughness and variable wettability. We anticipate that this model can be extended to dynamic scenarios, such as droplet spreading or impaction, in the future.

Key words: drops, contact lines, computational methods

1. Introduction

The task of calculating the equilibrium shape of a sessile droplet on an arbitrary surface, including the effects of gravity, is surprisingly difficult, despite the simplicity of the

problem description. In the simplest case of a flat horizontal surface, one can proceed by solving the Young–Laplace equation for the droplet shape given the droplet volume and the prescribed contact angle (Danov *et al.* 2016). However, even for a similar geometry such as an inclined plane, the lack of rotational symmetry leads to numerous additional complications that make the problem considerably more challenging. In particular, the boundary of the wetted area on the substrate (the contact line) is then completely unknown, as is the contact angle at each point on this boundary. Therefore, certain approximations are often made to make progress on this more difficult problem, such as assuming a circular contact line (Brown, Orr & Scriven 1980; Tredenick *et al.* 2021), or using empirical models for the contact angle distribution around the contact line (Ravi Annapragada, Murthy & Garimella 2012). For a more general surface geometry, the challenges are even more stark, as deviations in surface topology lead to a highly non-trivial formulation, again with an unknown contact line location and unknown contact angles.

A related problem is to study the evolving shape of a droplet that has been released on a surface with a relatively low energy field, and to determine the dynamics of the droplet shape as it settles towards equilibrium. In addition to the inherent challenges described above for the sessile droplet, this time-dependent problem is further complicated by the unknown relationship between the speed of the contact line and the contact angle (Hocking 1992). For our purposes, we are interested in using this time-dependent framework as a means to compute shapes of sessile droplets on arbitrary surfaces.

Some promise is shown in this area by energy minimisation methods, although these methods do not incorporate viscous effects, or model the temporal behaviour of settling droplets (Jamali & Tafreshi 2021). In contrast, in this study, we develop a numerical method based on smoothed particle hydrodynamics (SPH) to tackle these challenging problems. In the context of computing shapes of sessile droplets, one advantage of our approach is that the geometry of the droplet at the contact line arises naturally as a consequence of the SPH formulation, rather than as an input to the model.

Smoothed particle hydrodynamics is a computational method for discretising fluid flow problems using ‘particles’ that carry information about the fluid, originally developed by Gingold & Monaghan (1977) and Lucy (1977), and more recently reviewed by Wang *et al.* (2016) and Ye *et al.* (2019), for example. The particles serve as interpolation nodes for fluid properties such as density and velocity. The particles are not stationary and not connected; rather, they are advected with the flow according to the fluid velocity field $\mathbf{v}(\mathbf{x}, t)$. This Lagrangian discretisation transforms partial differential equations for any given field value $\varphi(\mathbf{x}, t)$ into ordinary differential equations for each particle’s value $\varphi_i(t)$, coupled with the advection equation $d\mathbf{x}_i/dt = \mathbf{v}_i$ for the particle’s position \mathbf{x}_i . Provided that sufficiently many particles are used in the simulation, the particle properties can then be interpolated to reconstruct the full fields everywhere in the domain.

Since its inception, SPH has been applied to a wide variety of problems, including astrophysics (Springel 2010), coastal engineering (Barreiro *et al.* 2013), porous medium flow (Zhu & Fox 2001) and even blood flow in injured arteries (Müller *et al.* 2004). The key advantage of SPH in simulating droplet behaviour is that the scheme does not necessitate the tracking of the sharp interface between the liquid and the air. Indeed, it does not track the interface directly at all; instead, the interface is deduced *a posteriori* based on the density field.

Some practitioners of SPH introduce surface tension effects by means of the continuum surface force (CSF). This idea dates back to Brackbill, Kothe & Zemach (1992) (in general) and Morris (2000) (applied to SPH). The CSF method starts with the Young–Laplace pressure boundary condition at the liquid–gas interface, but translates the normal force per unit area on the interface into a force per unit volume throughout the liquid by means

of a smoothing function. That is, a force \mathbf{F}_{CSF} is introduced everywhere in the fluid

$$\mathbf{F}_{CSF} = \delta_{CSF}(\mathbf{x}) \sigma K(\mathbf{x}) \hat{\mathbf{n}}(\mathbf{x}), \quad (1.1)$$

where δ is the smoothing function (maximised at the interface, and vanishing away from it), σ is the surface tension, $K = -\nabla \cdot \hat{\mathbf{n}}$ is the curvature of the interface and $\hat{\mathbf{n}}(\mathbf{x})$ the unit normal of the interface, extended into the fluid (Morris 2000). The success of these methods hinges on robust calculation of the smoothing function and the unit normal ‘field’. Recent approaches (Vergnaud *et al.* 2022; Blank, Nair & Pöschel 2024; Antuono, Marrone & Colagrossi 2025) require kernel corrections, which increase the computational burden of the method significantly, and smoothing of the normal field, as well as special corrections for thin jets. The matter is further complicated when one considers contact angle effects for droplets on substrates – Chiron *et al.* (2019) resort to tracking the liquid–solid interface explicitly. This additional complexity yields accurate results; however, our aim is to produce a robust method applicable to droplet simulations on arbitrarily rough substrates. As such, we seek a method that is more computationally efficient and robust to interfaces with high curvatures, which we expect to be prevalent in our application.

We choose the SPH method because it provides the needed flexibility to model droplets with non-trivial shapes on complex substrates that would otherwise pose a significant challenge for interface tracking or fixed grid methods (Ye *et al.* 2019). In the spirit of this interface-free approach, in the past decade a modified SPH method has emerged in which the Young–Laplace pressure boundary condition at the free surface is replaced with inter-particle forces that mimic cohesion and adhesion, in what is known as the pairwise-force SPH method (PF-SPH).

Kordilla, Tartakovsky & Geyer (2013), Tartakovsky & Panchenko (2016) and Shigorina, Kordilla & Tartakovsky (2017) all used a PF-SPH method to study droplet shapes on rough surfaces, although each used a different function for the pairwise force. Santacruz-Yunga *et al.* (2025) use a potential based on the popular Lennard–Jones potential for the pairwise interactions, which in this framework is analogous to a pairwise force. There is, in general, a lack of consensus regarding the best pairwise-force formulation, and a lack of understanding about what effect the formulation has on the simulated surface tension and contact angle. Existing pairwise-force profiles in the literature are rarely physically motivated and seldom investigated in their own right. Nevertheless, the PF-SPH method is very attractive for its simplicity, computational efficiency and robustness to thin features of both substrates and droplets. With this in mind, our main contribution is to propose a new force profile for PF-SPH that is physically motivated, scale-independent and carefully validated through the reproduction of multiple independent physical phenomena. To this end, we have developed a new method for calibrating the contact angle on an ideal surface by fitting whole droplet shapes obtained from semi-analytical solutions to the Young–Laplace equation. With the new PF-SPH model thoroughly calibrated and validated, we then demonstrate its application to several important test problems from the literature. First, we calculate the equilibrium shape of settling droplets on microscopically rough and chemically patterned substrates. Then, we apply the model to simulate a scenario from an agricultural application: a droplet impacting and settling on a virtual plant leaf.

The paper is structured as follows. In §2 we outline the details of our weakly compressible pairwise-force SPH model. We describe a new, scale-independent, pairwise-force term, and give some details on boundary handling, time integration and computational implementation. Several validation tests are carried out in §3, in which we ensure the model reproduces expected interfacial phenomena in both static and dynamic scenarios. In particular, in §3.3 we detail our method of calibrating the pairwise force to semi-analytical solutions for droplet shapes on flat surfaces. Section 4 is then devoted

to some numerical experiments of interest. Firstly, we simulate two small ($3\ \mu\text{l}$) droplets with different initial velocities on a surface with regular, sharp, square pillars, reproducing the experimental results of Dupuis & Yeomans (2005) and showing a transition between wetting states. Next, we simulate a droplet settling on a flat, hydrophobic, surface with a hydrophilic stripe, and observe a smooth transition in the droplet's contact angle from the equilibrium hydrophobic contact angle to the equilibrium hydrophilic contact angle. We then simulate a droplet settling on a virtually reconstructed wheat leaf surface in the context of broader work on understanding spray–canopy interactions on plants (Dorr *et al.* 2015, 2016; Mayo *et al.* 2015; Tredenick *et al.* 2021). We note that our PF-SPH scheme is quite flexible and should be applicable to a broad range of time-dependent droplet-related problems on complex substrates such as droplet impaction and spreading. Finally, the Julia code containing our implementation of the model is [available online](#) on GitHub.

2. Numerical formulation

2.1. Governing equations

The continuum model we use is the weakly compressible, barotropic Navier Stokes equations

$$\frac{D\rho}{Dt} = -\rho(\nabla \cdot \mathbf{v}), \quad (2.1)$$

$$\frac{D\mathbf{v}}{Dt} = \frac{-1}{\rho} \nabla P + \frac{\mu}{\rho} \nabla^2 \mathbf{v} + \mathbf{g} + \mathbf{F}^{(pf)}, \quad (2.2)$$

with \mathbf{x} the position, \mathbf{v} the velocity, ρ the density, P the pressure, μ the dynamic viscosity and \mathbf{g} the gravitational acceleration. The main focus of this work will be the body force (per unit mass) $\mathbf{F}^{(pf)}$, which we will construct in § 2.4 to reproduce surface tension and contact angle effects. The derivative D/Dt is the Lagrangian derivative

$$\frac{D}{Dt} = \frac{\partial}{\partial t} + \mathbf{v} \cdot \nabla, \quad (2.3)$$

which, as we shall see, lends itself naturally to discretisation using SPH.

2.2. Discretisation

As is standard in SPH methods, we represent the fluid by N particles, each with their own position, velocity, density and label (to distinguish fluid from solid, for example). Using i and j as particle indices, the discretised SPH form of the model (2.1)–(2.2) is

$$\frac{d\rho_i}{dt} = \rho_i \sum_{j=1}^N (\mathbf{v}_{ij} \cdot \nabla_i W_{ij}) V_j, \quad (2.4)$$

$$\frac{d\mathbf{v}_i}{dt} = \frac{-1}{\rho_i} \sum_{j=1}^N (P_i + P_j - \Pi) \nabla_i W_{ij} V_j + \mathbf{g} + \mathbf{F}_i^{(pf)}, \quad (2.5)$$

$$\frac{d\mathbf{x}_i}{dt} = \mathbf{v}_i,$$

$$\Pi = 2(d+2)\mu \frac{\mathbf{v}_{ij} \cdot \mathbf{x}_{ij}}{\|\mathbf{x}_{ij}\|^2},$$

$$P_i(\rho_i) = \frac{c_0^2 \rho_0}{7} \left[\left(\frac{\rho_i}{\rho_0} \right)^7 - 1 \right], \quad (2.6)$$

where $\mathbf{x}_{ij} = \mathbf{x}_i - \mathbf{x}_j$ for notational convenience, $W_{ij} = W(\mathbf{x}_{ij}; H)$ is an SPH kernel with compact support radius H , $V_j = m_j/\rho_j$ is the volume of particle j and d is the spatial dimension (always equal to 3 in this work). The pressure P_i is calculated from the density ρ_i with the equation of state (2.6). The constants c_0 and ρ_0 are the artificial speed of sound and the reference density, respectively. Note that we have switched from using the material derivative D/Dt to the total derivative d/dt , as the time derivative of a particle's property follows the flow by definition.

In this work we use the quintic Wendland function (Wendland 1995) as the SPH kernel, which we parameterise by H , its radius of support, also called the kernel cutoff radius

$$W(\mathbf{x} - \mathbf{x}'; H) = \frac{21}{2\pi H^3} w(\|\mathbf{x} - \mathbf{x}'\|/H),$$

$$w(\tau) = \begin{cases} (1 - \tau)^4(4\tau + 1), & 0 \leq \tau < 1, \\ 0, & \tau \geq 1. \end{cases} \quad (2.7)$$

Wendland functions were developed independently of SPH for their smoothness properties, but have been found to give accurate and stable SPH results (Dehnen & Aly 2012). In the literature, this kernel is sometimes parameterised by its smoothing length h , which is defined as half the kernel cutoff radius. To avoid this confusion, we parameterise the kernel by its cutoff, which we denote H , and set $H/\Delta x = \kappa = 4$, where Δx is the particle width.

With the exception of the pairwise-force term $\mathbf{F}^{(pf)}$, which will be the main focus of this work, the discretisation summarised above is well established in the literature: see, for example, Monaghan (2005). In this work we will implement and validate a new form of the pairwise-force term to model surface tension and contact angle effects, and highlight some particular properties of $\mathbf{F}^{(pf)}$ that yield stable and accurate simulations of droplets.

2.2.1. Continuity equation

The operator we use for the divergence of velocity is from Monaghan (2005)

$$\nabla \cdot \mathbf{v} = - \sum_{j=1}^N (\mathbf{v}_{ij} \cdot \nabla_i W_{ij}) V_j, \quad (2.8)$$

and is specifically constructed to vanish when \mathbf{v} is constant.

2.2.2. Pressure gradient and equation of state

The discretisation of the gradient of pressure that we use, namely

$$(\nabla P)_i = \sum_{j=1}^N (P_i + P_j) \nabla_i W_{ij} V_j, \quad (2.9)$$

is due to Bonet & Lok (1999) (and recently used by Domínguez *et al.* (2022)), who showed it to be consistent with (2.4) and to conserve linear momentum exactly. Note that since $\nabla_i W_{ij} = -\nabla_j W_{ji}$, we have the anti-symmetry $(\nabla P)_i = -(\nabla P)_j$. This is the property that conserves momentum, since the contribution of particle j to $d\mathbf{v}_i/dt$ is equal and opposite to the contribution of particle i to $d\mathbf{v}_j/dt$.

The pressure is calculated from the density by the equation of state. We follow Monaghan (1994, 2005) in using

$$P_i = \frac{c_0^2 \rho_0}{7} \left[\left(\frac{\rho_i}{\rho_0} \right)^7 - 1 \right], \quad (2.10)$$

which was originally reported by Cole (1948, p. 44) in the study of underwater explosions. Cole notes that they chose the exponent 7 to approximately fit experimental data. In our case, we find that the results are not at all sensitive to the particular equation of state in use – even the first-order approximation $P(\rho) = c_0^2(\rho - \rho_0)$ gives almost indistinguishable results. The coefficient c_0 is an artificial speed of sound that controls the compressibility of the fluid. The actual speed of sound in water is around 1500 m s^{-1} , but such a value would require the use of extremely small time steps to properly resolve pressure waves travelling at that speed. Instead, in the weakly compressible model, we use an artificial value of c_0 of the order of 100 m s^{-1} such that density fluctuations are kept to within 1 % of the reference value ρ_0 (Monaghan 2005). The artificial speed of sound required for a particular problem can be estimated as $10v_{\max}$, an order of magnitude greater than the maximum expected fluid speed.

2.2.3. Viscosity

The discrete operator we use to approximate the Laplacian is that of Monaghan & Gingold (1983), namely

$$(\nabla^2 \mathbf{v})_i = 2(d+2) \sum_{j=1}^N \frac{\mathbf{v}_{ij} \cdot \mathbf{x}_{ij}}{\|\mathbf{x}_{ij}\|^2} \nabla_i W_{ij} V_j, \quad (2.11)$$

where d is the spatial dimension. More recently proposed operators exist with favourable properties, but we have chosen this particular discretisation based on the analysis by Colagrossi, Antuono & Le Touzé (2009) that suggests it is more appropriate for the simulation of free surfaces.

2.2.4. Solid boundary treatment

At the fluid–solid interface, we have the no-slip condition: $\mathbf{v} = \mathbf{0}$. We impose this condition indirectly, representing the solid substrate with fixed dummy particles, initialised on a regular grid with spacing Δx . Multiple layers of these particles are used to avoid an SPH neighbourhood deficiency at the boundary. The solid particles have the same physical properties as the fluid at rest, with mass $\rho_0 \Delta x^3$ and density ρ_0 , but with zero velocity. This simple approximation of the no-slip condition has been shown to be consistent in the limit as $H \rightarrow 0$, although does not reproduce it exactly in simulations. Other schemes utilise mirroring approaches (Macia *et al.* 2011), in which fluid properties are interpolated and extended into the solid boundary using surface normals. In our study of droplets on rough surfaces, however, this approach would be quite complex to implement for a general surface. For example, it is not straightforward to map any point in space to its closest surface point and thus the appropriate surface normal. Furthermore, some boundary points may be assigned incorrect properties because their associated interpolation point above the solid is in the gas phase, which we do not discretise with SPH particles. The subject of more accurate boundary condition treatment is thus left to future work, and the interested reader is referred to Macia *et al.* (2011) for more details.

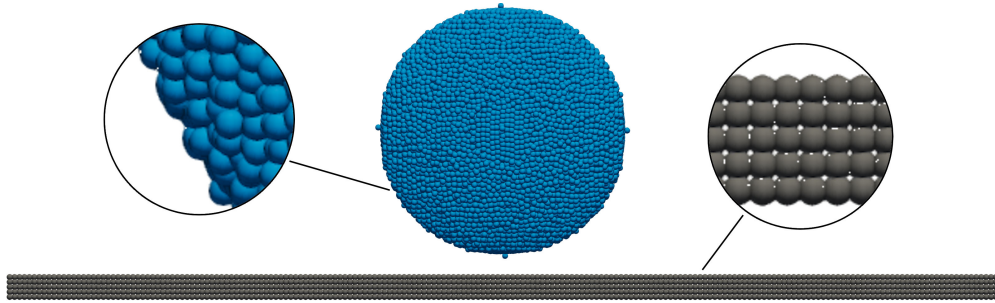


Figure 1. A side view of a three-dimensional particle simulation in which a droplet of fluid particles (blue) is about to impact solid boundary particles (grey). Insets show closeups of each type of particle. Fluid particles are advected with the flow and thus disorganised, while solid particles are fixed on a cubic lattice. The particles are rendered as spheres of volume m_j/ρ_j , but we note that this is for visualisation only: in the SPH scheme, they are better understood as interpolation nodes.

The ‘dummy’ solid particles are included in the summations over j in the discrete continuity and momentum (2.4) and (2.5), as if they were fluid particles. Pressure forces and the repulsion due to pairwise forces ensure that fluid particles do not penetrate the boundary. Figure 1 shows a typical set-up in which a droplet of fluid particles is about to impact a flat solid boundary.

2.2.5. Time integration

The time integration scheme we use is a second-order, symplectic, position-Verlet scheme. It is modified from Leimkuhler & Matthews (2015) by Domínguez *et al.* (2022) to include a velocity half-step, which is necessary to integrate the continuity equation and calculate the viscous term. We will use the following notation for the discretised governing equations (2.1) and (2.2):

$$\frac{d\rho_i}{dt} := Q_i, \quad \frac{d\mathbf{v}_i}{dt} := \mathbf{A}_i. \quad (2.12)$$

Dropping particle indices for clarity, and letting the value of a quantity φ at time step k be denoted $\varphi^{(k)}$, the original position-Verlet scheme (Leimkuhler & Matthews 2015, p. 107) reads

$$\begin{aligned} \mathbf{x}^{(k+\frac{1}{2})} &= \mathbf{x}^{(k)} + \frac{\Delta t}{2} \mathbf{v}^{(k)}, \\ \mathbf{v}^{(k+1)} &= \mathbf{v}^{(k)} + \Delta t \mathbf{A}^{(k+\frac{1}{2})}, \\ \mathbf{x}^{(k+1)} &= \mathbf{x}^{(k+\frac{1}{2})} + \frac{\Delta t}{2} \mathbf{v}^{(k+1)}. \end{aligned} \quad (2.13)$$

However, the viscous term in $\mathbf{A}^{(k+(1/2))}$ involves the velocity at the half time step, so Domínguez *et al.* (2022) introduce the intermediate step

$$\mathbf{v}^{(k+\frac{1}{2})} = \mathbf{v}^{(k)} + \frac{\Delta t}{2} \mathbf{A}^{(k)}. \quad (2.14)$$

Simplifying the expression for $\mathbf{x}^{(k+1)}$, and including the integration of the continuity equation, the full scheme reads

$$\begin{aligned} & \text{Calculate } \mathbf{A}^{(k)} \text{ and } Q^{(k)}, \\ & \mathbf{x}^{(k+\frac{1}{2})} = \mathbf{x}^{(k)} + \frac{\Delta t}{2} \mathbf{v}^{(k)}, \\ & \mathbf{v}^{(k+\frac{1}{2})} = \mathbf{v}^{(k)} + \frac{\Delta t}{2} \mathbf{A}^{(k)}, \\ & \rho^{(k+\frac{1}{2})} = \rho^{(k)} + \frac{\Delta t}{2} Q^{(k)}, \end{aligned} \quad (2.15)$$

$$\begin{aligned} & \text{Calculate } \mathbf{A}^{(k+\frac{1}{2})} \text{ and } Q^{(k+\frac{1}{2})}, \\ & \mathbf{v}^{(k+1)} = \mathbf{v}^{(k)} + \Delta t \mathbf{A}^{(k+\frac{1}{2})}, \\ & \mathbf{x}^{(k+1)} = \mathbf{x}^{(k)} + \frac{\Delta t}{2} [\mathbf{v}^{(k)} + \mathbf{v}^{(k+1)}], \\ & \rho^{(k+1)} = \rho^{(k)} + \Delta t Q^{(k+\frac{1}{2})}. \end{aligned} \quad (2.16)$$

The time step is chosen adaptively according to viscous, maximum force and acoustic constraints

$$\begin{aligned} \Delta t_v &= \frac{\Delta x^2 \rho_0}{\mu}, \quad \Delta t_a = 0.15 \sqrt{\frac{\Delta x}{\max_j \|\mathbf{A}_j\|}}, \quad \Delta t_c = 0.15 \frac{\Delta x}{c_0}, \\ \Delta t &= \min(\Delta t_v, \Delta t_a, \Delta t_c). \end{aligned} \quad (2.17)$$

In the present application, the acoustic constraint determining Δt_c is almost always far smaller than the other two in (2.17), due to the small scale of the droplets and the comparatively large artificial speed of sound c_0 .

2.3. Implementation details

The Lagrangian nature of SPH, while making it a very flexible method, also makes it challenging to implement efficiently. We follow the work of Ihmsen *et al.* (2011) in the use of some key data structures and parallel methods, which we will briefly summarise here.

Implemented naively, each sum in the discretised equations (2.4) and (2.5) has a time complexity of $\mathcal{O}(N^2)$. This is made more efficient by pre-computing a neighbour list

$$\mathcal{J}(i) = \{j : \|\mathbf{x}_i - \mathbf{x}_j\| < H\}, \quad (2.18)$$

for each fluid particle i . Any sum over $j = 1, \dots, N$ then becomes a sum over $j \in \mathcal{J}(i)$. Since density fluctuations are small in this weakly compressible scheme, the number of neighbours is approximately constant (around $4\pi\kappa^3/3$). Thus, the complexity of calculating the particle interactions becomes $\mathcal{O}(N)$.

We accelerate the neighbour search by using a background grid with cells of width H . Each grid cell is uniquely identified by a tuple of integer coordinates (c_1, c_2, c_3) , and we keep a hash table of lists of particles contained in each cell. To minimise memory allocations, we pre-allocate enough storage for each of these lists to contain κ^d indices. Density fluctuations are low, so the maximum number of fluid particles that one cell may contain is roughly constant. The neighbour search then only considers particles in neighbouring cells (the number of which is roughly constant), therefore reducing the time complexity to $\mathcal{O}(N)$.

Finally, we make use of shared memory parallelism with many CPU cores wherever possible. The particle–particle interactions are calculated in parallel, as are the neighbour lists. For more optimisation details we refer the interested reader to Ihmsen *et al.* (2011) for CPU implementations, or for GPU implementations see Domínguez *et al.* (2011), Crespo *et al.* (2011, 2015) and Domínguez *et al.* (2022). Simulations were run using up to 64 processors in parallel.

2.4. Pairwise-force model for interfacial phenomena

Surface tension and wetting are both effects of intermolecular forces (Bormashenko 2017). A molecule at an interface misses approximately half of its interactions with neighbours when compared with a molecule in the bulk, and the resulting imbalance of forces leads to free-surface energy. For surface tension, the relevant forces are cohesive (fluid–fluid interactions) while, for wetting, the relevant forces are adhesive (fluid–solid interactions). Depending on the relative strengths of these forces, a droplet could be almost spherical, spread to completely wet a solid or any configuration in between, to minimise the free-surface energy.

We aim to reproduce this behaviour on a much larger scale by mimicking intermolecular forces between SPH particles. This is conceptually similar to the Lennard–Jones potentials used in molecular dynamics simulations (Jones 1924). The basis for these forces in SPH is empirical; nevertheless, in § 3 we will show that the pairwise-force SPH model reproduces interfacial phenomena consistently and predictably.

The pairwise particle interaction forces are included in the momentum equation (2.5) via the term $\mathbf{F}_i^{(pf)}$

$$\mathbf{F}_i^{(pf)} = \frac{H}{m_i} \sum_{j=1}^N s_{ij} f_{ij}(\|\mathbf{x}_{ij}\|/H) \frac{\mathbf{x}_{ij}}{\|\mathbf{x}_{ij}\|}, \quad (2.19)$$

where s_{ij} controls the strength of the pairwise force between particles i and j . Following the analogy with intermolecular potentials, we construct the pairwise-force profile $f_{ij}(\|\mathbf{x}_{ij}\|/H)$ to be repulsive at short distances (less than one particle width), attractive at medium distances and vanish outside the SPH kernel support radius, H . In other works, this term has been constructed as a combination of Gaussians (Tartakovsky & Panchenko 2016), SPH kernels (Kordilla *et al.* 2013; Shigorina *et al.* 2017) or part of a cosine curve (Tartakovsky & Meakin 2005; Nair & Pöschel 2018). For simplicity, we will instead use polynomials for the force profile, with some intuitive constraints at key points. Those constraints are

$$\begin{aligned} f_{ij}(0) &= 1, & (\text{avoid trivial solution}) \\ f'_{ij}(0) &= f'_{ij}(1) = 0, & (\text{smoothness at endpoints}) \\ f_{ij}(1) &= 0, & (\text{continuity at kernel support radius}) \\ f_{ij}(\kappa^* \Delta x/H) &= 0. & (\text{repulsion-to-attraction point}) \end{aligned} \quad (2.20)$$

The last constraint, controlling the zero crossing of the force profile, is intentionally different for the fluid–fluid (ff) and the fluid–solid (fs) interactions. We choose κ^* to be 1.1 and 2 for the fluid–fluid and the fluid–solid interactions, respectively. The fluid–fluid force profile is attractive at a shorter distance than the fluid–solid to prioritise cohesion over adhesion for stability at the contact line.

We have chosen the zero crossing of the fluid–fluid pairwise-force curve to be approximately the ‘rest distance’ of the particles. To do this, we imagine optimally packed spheres in a face-centred cubic layout. The Voronoi diagram of this arrangement is

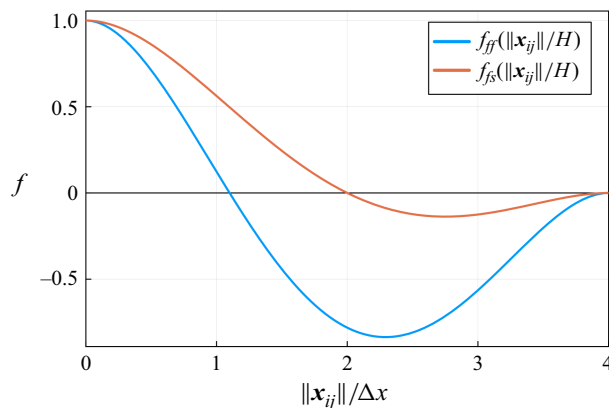


Figure 2. Distance-dependent pairwise-force profiles f_{ff} and f_{fs} over the kernel support, $\tau \in [0, 1]$ or $\|\mathbf{x}_{ij}\|/\Delta x \in [0, \kappa]$. Positive values indicate repulsion and negative values indicate attraction. Note that we have plotted the force profiles with respect to the particle width Δx rather than the dimensionless τ , to highlight the physically motivated choice of zero crossing discussed in § 4.4.

the rhombic dodecahedral honeycomb. If we equate the volume of one of our particles $((\Delta x)^3)$ with the volume of a rhombic dodecahedron, we find that the distance between neighbouring particles in such a packing is approximately $1.1\Delta x$. This is the geometric motivation behind the location of the zero crossing of the force profile in (2.19).

The minimum degree of a polynomial satisfying our five constraints is four, and so we have

$$f_{ij}(\tau) = \begin{cases} 1 + \alpha_{ij}\tau^2 - 2(2 + \alpha_{ij})\tau^3 + (3 + \alpha_{ij})\tau^4, & 0 \leq \tau \leq 1, \\ 0, & \tau > 1, \end{cases} \quad (2.21)$$

where we use $\alpha_{ff} = -23.5$ for fluid–fluid interactions, and $\alpha_{fs} = -11$ for fluid–solid interactions, to satisfy the zero crossing constraints above. Figure 2 shows these force profiles over the range of possible particle distances.

The parameter s_{ij} in (2.19) controls the strength of the pairwise force and, like $f_{ij}(\tau)$, depends on the labels of the particles i and j : fluid or solid. We denote the cohesive force strength s_{ff} (fluid–fluid) and the adhesive force strength s_{fs} (fluid–solid). Note the inclusion of the length scale H in the form of $\mathbf{F}_i^{(pf)}$ in (2.19): this is a departure from established pairwise-force methods (Kordilla *et al.* 2013; Nair & Pöschel 2018; Tartakovsky & Meakin 2005; Liu, Meakin & Huang 2006; Tartakovsky & Panchenko 2016; Shigorina *et al.* 2017; Arai *et al.* 2020), which have a scale dependency on H . Our approach ensures that the units of s are that of an interfacial tension. Taking $f_{ij}(\tau)$ to be dimensionless, the units of (2.19) are

$$\begin{aligned} [\text{ms}^{-2}] &= [\text{m}][\text{kg}^{-1}]s_{ij}[1][\text{m}][\text{m}^{-1}], \\ s_{ij} &= [\text{Nm}^{-1}]. \end{aligned} \quad (2.22)$$

Thus, the units of s are Nm^{-1} , analogous to the true surface tension σ , which ensures the simulated surface tension is independent of the resolution.

While the PF-SPH model may seem an oversimplification of the complex (and small-scale) behaviour that is molecular cohesion and adhesion, it is best thought of as a coarse approximation of these phenomena, at the resolution of the SPH discretisation. We will show in the next section that the resulting surface tension is linearly related to

the pairwise-force strength s_{ff} , and that this simple model captures complex behaviour in a predictable way.

3. Validation of numerical scheme

In this section we present three validation tests to verify that the pairwise-force model correctly reproduces surface tension and contact angle effects. These tests not only validate the model's ability to reproduce interfacial phenomena, they also serve to calibrate the model parameters s_{ff} and s_{fs} to the material properties of interest – the surface tension σ (a property of the liquid) and equilibrium contact angle θ_{CA} (a property of the liquid–substrate pair).

3.1. Laplace pressure

The first test we use will validate the surface tension of the fluid in a static scenario, independent of fluid–solid interactions. The Young–Laplace equation describes the difference in pressure ΔP due to surface tension σ in a spherical droplet of radius R (Bormashenko 2017)

$$\Delta P = \frac{2\sigma}{R}. \quad (3.1)$$

By testing the pressure difference at different droplet radii for a fixed inter-particle force strength s_{ff} , we can calibrate (and validate) the resulting surface tension σ . Given that we only model the fluid phase, and therefore have $P_{out} = 0$, we need only calculate P_{in} . We do this by borrowing a technique from molecular dynamics, calculating the total pressure from a many-body simulation (Hoover 1998). When calculated this way, the pressure due to particle–particle interactions is called the virial pressure, and is defined by Allen & Tildesley (1989), Tartakovsky & Meakin (2005) as

$$P(r) = \frac{1}{2dV(r)} \sum_{i \in \mathcal{I}(r)} \sum_{j=1}^N \mathbf{F}_{ij} \cdot (\mathbf{x}_i - \mathbf{x}_j), \quad (3.2)$$

where d is the spatial dimension (taken here to be $d = 3$), $V(r)$ is the volume of a sphere of radius r and \mathbf{F}_{ij} is the sum of the pressure force and pairwise force that particle i experiences due to particle j . The outer summation (over i) includes only particles in the set $\mathcal{I}(r)$ of particles within a distance r of the centre of the droplet. This so-called virial radius $r < R$ is used in place of the actual droplet radius R to exclude the region near the interface (Tartakovsky & Meakin 2005). When $r = R$, we see a divergence of the pressure near the free surface due to the neighbourhood deficiency in the SPH approximations there. Figure 3 shows the virial pressure measured at different radii, with the pressure clearly diverging as r approaches R . For accurate estimates of the virial pressure we take an average of $P(r)$ over the interval $r \in [R - 3H, R - 2H]$. If $R \leq 4H$, we take $r = R - 2H$.

For the simulations, we initialise spherical droplets consisting of particles with properties given in table 1, in zero gravity. We randomly perturb each particle, by no more than $0.1\Delta x$, to speed up their rearrangement due to inter-particle forces $\mathbf{F}^{(pf)}$. We then allow the droplet to reach equilibrium over 200 ms before measuring the virial pressure. Figure 4 shows that the pairwise-force model reproduces the linear relationship $\Delta P \propto 2/R$; we can measure the surface tension at each value of s_{ff} as the slope of each of these lines. We also note that the standard deviation of the virial pressure over the range $r \in [R - 3H, R - 2H]$ is relatively small and thus does not introduce significant uncertainty in the calibrated surface tensions. Plotting the measured surface tension

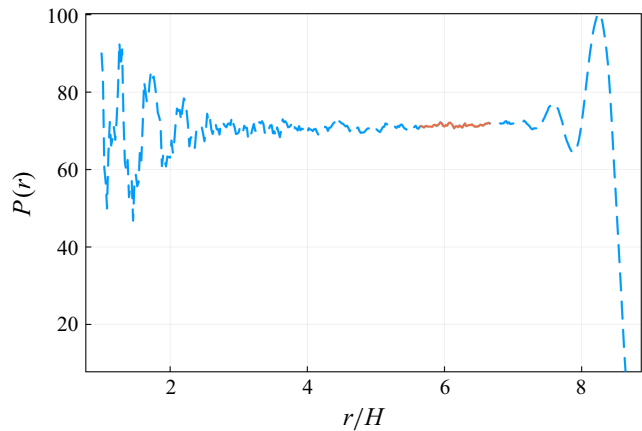


Figure 3. Virial pressure calculated using (3.2) at different radii r , given here in units of the kernel support radius H . The actual radius of this spherical droplet is 1 mm, approximately $8.5H$. The calculated virial pressure diverges for $r \gtrsim 6.5H$ due to the neighbourhood deficiency of the particles near the free surface. A red line shows the region over which we average $P(r)$.

Property	Value(s)
Density, ρ_0	10^3 kg m^{-3}
Viscosity, μ	$0.89 \text{ mPa} \cdot \text{s}$
Speed of sound, c_0	60 m s^{-1}
Radius, R	$[0.8, 1.2] \text{ mm}$
s_{ff}	$[0, 2 \times 10^{-3}] \text{ N m}^{-1}$
Resolution, H	$1.2 \times 10^{-4} \text{ m}$
No. of particles	$[79\,400, 268\,000]$

Table 1. Fluid properties in Laplace pressure simulations.

against the model parameter s_{ff} reveals a simple linear relationship in figure 5, namely

$$\sigma = 30.96 s_{ff}. \tag{3.3}$$

This is consistent with the dimensional analysis in § 2.4, and makes the prescription of surface tension in the model very simple. We have tested this relationship for particle width Δx as small as $2 \times 10^{-5} \text{ m}$ and as large as $8 \times 10^{-5} \text{ m}$ and found it to be independent of the resolution, as expected.

3.2. Oscillating droplets

With the surface tension now calibrated in a static scenario, we next validate the model for surface tension in a dynamic scenario. For this task we choose to study the oscillation of a free droplet that has been perturbed from its spherical equilibrium. The linear frequency of oscillation of an inviscid droplet (in the eigenmode of interest) was found by Rayleigh (1879) (with a more succinct derivation given by Landau & Lifshitz (1987)) to be

$$f = \frac{1}{\pi} \sqrt{\frac{2\sigma}{R^3 \rho}}. \tag{3.4}$$

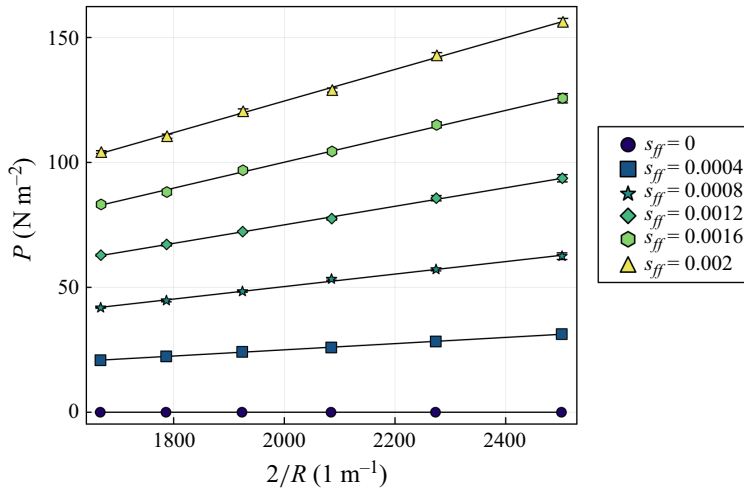


Figure 4. Laplace pressure validation using calculated virial pressures of spherical droplets. For different values of the cohesive force strength s_{ff} , the pressure follows $P \propto 2/R$, where R is the radius of the droplet. Markers show measurements from simulations, and black lines show linear fits. Error bars show standard deviations of the virial pressure across the virial radii $r \in [R - 3H, R - 2H]$. The slope of each line gives the surface tension σ for the corresponding s_{ff} .

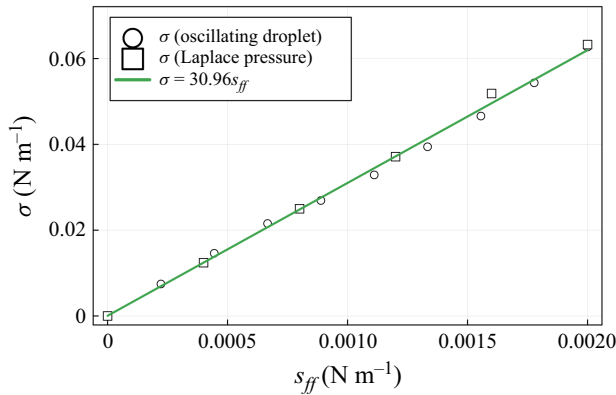


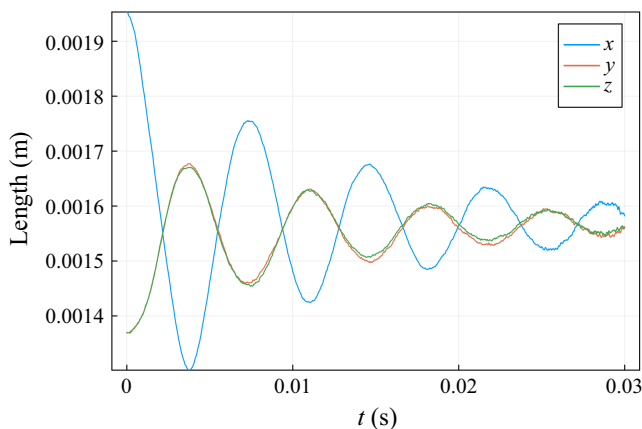
Figure 5. Calibrating the cohesive force strength s_{ff} to measured surface tension in two different tests. Circles show surface tensions calculated from the Laplace pressure $P = 2\sigma/R$ (see figure 4). Squares show surface tensions calculated from ellipsoidal droplet oscillations (e.g. figure 6). The fitted line shows a simple linear relationship between s_{ff} and the surface tension.

With material properties given in table 2, we initialise a spherical droplet of radius 0.788 mm with particles that we randomly perturb by no more than $0.1\Delta x$, and allow the particle distribution to settle for 1 ms. Then we ‘stretch’ the spherical droplet into an ellipsoid with the coordinate transform

$$\mathbf{x} \leftarrow \underbrace{\frac{1}{\sqrt[3]{abc}} \begin{bmatrix} a & 0 & 0 \\ 0 & b & 0 \\ 0 & 0 & c \end{bmatrix}}_T \mathbf{x}. \quad (3.5)$$

Property	Value(s)
Density, ρ_0	1000 kg m ⁻³
Viscosity, μ	0
Speed of sound, c_0	100 m s ⁻¹
Volume, V	2.05 μ l
s_{ff}	[0, 2] mN m ⁻¹
Resolution, H	1.2×10^{-4} m
No. of particles	75 993

Table 2. Fluid properties in oscillating droplet simulations.


Figure 6. The oscillating diameters of an inviscid, axis-aligned ellipsoidal droplet over 30 ms, for $s_{ff} = 0.00156$. Material properties are given in [table 2](#).

Since $\det(T) = 1$, this transformation preserves volume, and therefore density of the fluid particles. The elements a , b , c are the relative lengths of the ellipsoid's semi-axes, which we take to be 1.0, 0.7 and 0.7, respectively.

The simulation then proceeds, with the diameter of the droplet oscillating over 3 ms as shown in [figure 6](#) for $s_{ff} = 0.00156$ (corresponding to $\sigma = 47$ mN m⁻¹). Despite the fluid having zero viscosity in the simulation, the oscillations are clearly damped – the amplitude decreases with each oscillation. Nair & Pöschel (2018) investigate possible causes of this damping, finding that some of the system's energy is dissipated as the particles arrange themselves into a crystal-like lattice.

Despite these effects, we can recover the frequency of the oscillations to determine the surface tension of the droplet. A discrete Fourier transform of the oscillations ([figure 7](#)) shows a peak at 138 Hz. With (3.4), we can calculate the surface tension as $\sigma = 47$ mN m⁻¹ when $s_{ff} = 0.00156$. [Figure 5](#) shows the surface tensions calculated this way, plotted against the cohesive force $s_{ff} \in [0, 0.002]$, corroborating the linear relationship from the Laplace pressure test in § 3.1. Thus, we have shown in two independent tests – one static and the other dynamic – that the surface tension induced by the pairwise forces scales linearly with the interaction strength parameter s_{ff} .

3.3. Young–Laplace profile fitting for contact angle

Having calibrated and validated the surface tension in both static and dynamic scenarios, we now turn our attention to wetting phenomena and the adhesive force strength s_{β} .

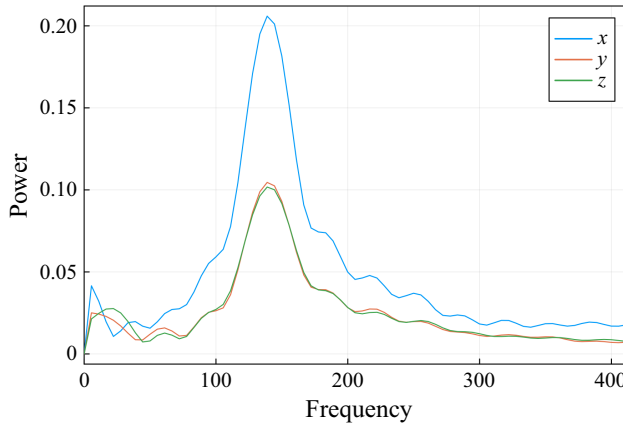


Figure 7. The power spectrum of the oscillating droplet's diameters (see figure 6), with a peak at 138 Hz, which gives $\sigma = 47 \text{ mN m}^{-1}$ when $s_{ff} = 0.00156$ from equation (3.4).

The angle that a droplet's liquid–gas interface makes with its liquid–solid interface – the contact angle – is commonly used to measure the ability of the liquid to wet the solid (Bormashenko 2017). This angle is often measured experimentally by drawing a tangent line to the liquid–gas interface where it meets the solid; however, this would seem only to validate the model in the immediate vicinity of the contact line. Instead, we will use semi-analytical solutions for whole droplet shapes to validate the model and calibrate the adhesive force to the contact angle.

For this test, we initialise a spherical droplet at a distance of H (the kernel support radius) above a flat solid surface, with a thickness of H , to ensure the neighbourhood of a fluid particle near the boundary is not deficient. In all the contact angle simulations, the fluid particles have density 1000 kg m^{-3} , viscosity $0.89 \text{ mPa} \cdot \text{s}$ and artificial speed of sound 100 m s^{-1} . We have simulated droplets of various surface tensions, volumes, and resolutions to ensure the model is not scale-dependent. Initially, the fluid particles are perturbed by no more than $0.1\Delta x$ and the particle distribution is allowed to settle for 1 ms under zero gravity, without interacting with the surface. Then, we switch on gravity ($g = -9.81 \text{ m s}^{-2}$), allowing the droplet to fall and spread across the solid surface. After 50 ms, the droplet settles and we are ready to extract the liquid–gas interface.

The liquid–gas interface of an SPH-simulated droplet is an isosurface of the density field defined by the SPH interpolation $\langle \rho(\mathbf{x}) \rangle$

$$\mathcal{S} = \left\{ \mathbf{x} : \sum_{j \in \mathcal{I}_f} m_j W(\mathbf{x} - \mathbf{x}_j; H) = \frac{\rho_0}{2} \right\}, \quad (3.6)$$

where \mathcal{I}_f is the index set of fluid particles. We realise the implicit surface \mathcal{S} using the marching cubes algorithm, with a grid spacing of $0.1\Delta x$. Then, to determine the contact angle of the droplet, we fit the shape of an axisymmetric sessile droplet determined by the Young–Laplace (Y–L) equation (Danov *et al.* 2016) to the vertices of the SPH droplet isosurface in cylindrical polar coordinates (R_j, Z_j) where the origin is given by the droplet's centre of mass.

In order to fit the data points to the Y–L surface we minimise the function

$$L(\theta_{CA}, Z_{shift}) = \sum_j \frac{1}{R_j + \epsilon} \text{mindist}(R_j, Z_j - Z_{shift}; \theta_{CA})^2, \quad (3.7)$$

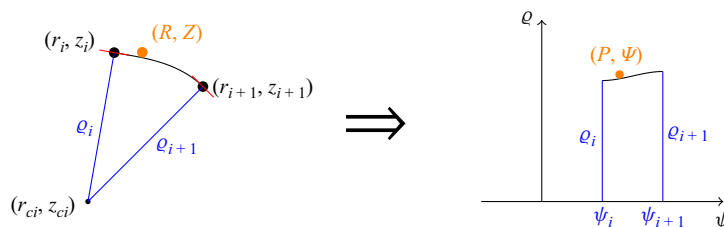


Figure 8. Schematic of the transformation from the cylindrical polar world coordinates to the local polar coordinates of a surface segment.

where θ_{CA} is the contact angle, Z_{shift} is a vertical shift of the data position and $\text{mindist}(R, Z; \theta_{CA})$ is the minimum distance from the point (R, Z) to the Y–L surface for the specified volume, surface tension and contact angle. The circumference of the droplet, and therefore the number of expected isosurface vertices, increases linearly with R . Thus, to account for the varying density of the samples, we weight the errors with the factor $1/(R_j + \epsilon)$, where $\epsilon > 0$ is a small constant to avoid division by zero.

To construct the distance function $d(R, Z; \theta_{CA})$ we must first compute the Y–L droplet shape for a given volume V_0 , surface tension σ and contact angle θ_{CA} . Following Danov *et al.* (2016) (using equations first reported by Hartland & Hartley (1976, p. 40)), we solve the system of ordinary differential equations

$$\begin{aligned} \frac{dr}{ds} &= \cos \theta, \\ \frac{dz}{ds} &= \sin \theta, \\ \frac{d\theta}{ds} &= \frac{2}{\mathcal{B}} - \frac{\sin \theta}{r} + \frac{\rho g}{\sigma} z, \\ \frac{dV}{ds} &= r^2 \sin \theta, \end{aligned} \quad (3.8)$$

from the ‘initial condition’ $r = z = \theta = V = 0$ until $\theta = \theta_{CA}$, where \mathcal{B} is the curvature at the apex of the droplet, chosen such that the correct volume is achieved. Numerically, the Y–L drop surface is given as a series of points (r_i, z_i) with their gradient as an angle θ_i .

We approximate the normal distance to the surface by transforming the coordinates for a given surface segment $(r_i, z_i) - (r_{i+1}, z_{i+1})$ into a local polar coordinate system

$$(\varrho, \psi) \rightarrow \left(\sqrt{(r_i - r_c)^2 + (z_i - z_c)^2}, \arctan \frac{z_i - z_c}{r_i - r_c} \right), \quad (3.9)$$

where the centre (r_c, z_c) is given by the intersections of two lines passing through each of the end points of the segment perpendicular to their gradients (figure 8). That is

$$r_c = \frac{\sin \theta_i (z_{i+1} - z_i) + \cos \theta_i (r_{i+1} - r_i)}{\sin \theta_i \cos \theta_{i+1} - \cos \theta_i \sin \theta_{i+1}} \sin \theta_i + r_i, \quad (3.10)$$

$$z_c = -\frac{\sin \theta_i (z_{i+1} - z_i) + \cos \theta_i (r_{i+1} - r_i)}{\sin \theta_i \cos \theta_{i+1} - \cos \theta_i \sin \theta_{i+1}} \cos \theta_i + z_i. \quad (3.11)$$

The surface location along the segment is then given by $\varrho_i(\psi) = \varrho_i + (\varrho_{i+1} - \varrho_i)(3t^2 - 2t^3)$, where $t = (\psi - \psi_i)/(\psi_{i+1} - \psi_i)$. The difference $P - \varrho_i(\psi)$ is taken as the approximation of the normal distance from the point (R, Z) to the segment. Therefore the minimum distance from the point (R, Z) to the surface is the minimum distance over

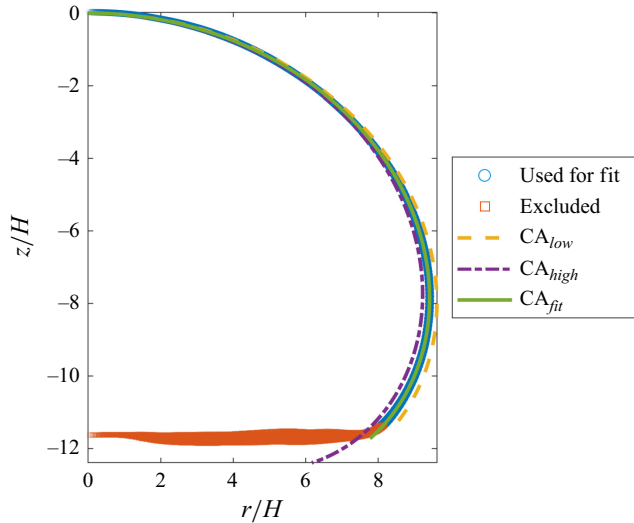


Figure 9. An example of a Y–L profile (a solution to the system (3.8)) fitted to an SPH droplet. Isosurface vertices are shown in cylindrical coordinates about the centre of the top of droplet. The solid line shows the profile of an axisymmetric droplet satisfying the Y–L equation, fit to the isosurface vertices with the contact angle as a free parameter. Dashed and dot-dashed lines show the extent of contact angles satisfying the fitting tolerance.

all segments for which the surface interpolation is valid

$$\text{mindist}(R, Z; \theta_{CA}) = \min_i \min_{\psi \in [\psi_i, \psi_{i+1}]} |P - \varrho_i(\Psi)|. \quad (3.12)$$

Figure 9 shows an example of an SPH droplet isosurface and its best fit Y–L shape. Also shown are the Y–L shapes for the contact angles θ_{low} and θ_{high} , such that $\theta_{CA} \in [\theta_{low}, \theta_{high}]$ and $L(\theta_{low}, Z_{shift}) = L(\theta_{high}, Z_{shift}) = \text{tol}$, a fitting tolerance. For each simulated droplet, this approach gives a feasible range of contact angles as well as the optimal fit. The results of measuring the contact angles of simulated droplets in this way are shown in figures 10 and 11, grouped by surface tension and volume, respectively, and plotted against the ratio s_{fs}/s_{ff} . The contact angles for different surface tensions and volumes coincide for equal values of this ratio, suggesting that the contact angle produced by the PF-SPH model is scale-independent and making the specification of the contact angle straightforward in practice. We find that for higher contact angles, where larger changes in θ_{CA} result in only small changes in the droplet profile, the feasible range $\theta_{high} - \theta_{low}$ is relatively large. For intermediate contact angles between 30° and 120° , however, the feasible region is smaller and we can be more precise in our specification of θ_{CA} via s_{fs} .

With this validation of the droplet shape and calibration of the contact angle, we now have a simple procedure for specifying the surface tension σ and contact angle θ_{CA} in the PF-SPH scheme. We can calculate the required cohesive strength $s_{ff} = \sigma/30.96$ from (3.3). Then we can interpolate the data from figure 10 to find the required ratio s_{fs}/s_{ff} , and, knowing s_{ff} , calculate s_{fs} .

4. Case studies and numerical experiments

In this section we demonstrate the versatility of our PF-SPH scheme by presenting some numerical experiments that are usually challenging for competing computational frameworks such as interface-tracking or grid-based methods. Of course, these problems are not intractable for such methods – see, for example, works such as Jansen *et al.* (2012)

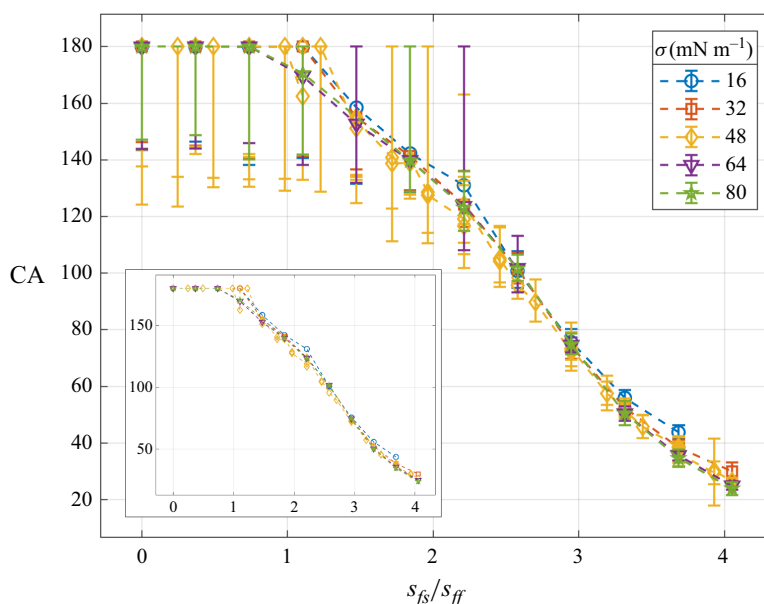


Figure 10. Contact angles, measured by fitting Y–L profiles to sessile droplet density isosurfaces, are plotted against the ratio of pairwise-force strengths, s_{fs}/s_{ff} , and grouped by surface tension. A droplet is excluded if the volume enclosed by the density isosurface differs from the actual droplet’s volume by more than 10 %. Inset: the curves without error bars, for clarity.

in which an interface-tracking method was used with a substrate with variable wettability, or Dupuis & Yeomans (2005) where a lattice-Boltzmann simulation was used with a rough substrate. The advantage of our approach that we shall highlight is that PF-SPH is capable of modelling droplets on chemically and physically heterogeneous substrates with little to no modifications to the scheme.

4.1. Microstructured surface

Synthetic surfaces with manufactured microscopic roughness attract interest from scientists and engineers alike for their potential commercial applications (e.g. self-cleaning surfaces, reduced drag on marine vessels, collecting freshwater from fog (Chamakos, Sema & Papathanasiou 2021)). Surfaces with sharp geometric features, however, are challenging to incorporate into computational models with explicit boundary conditions on the contact line. Here we will demonstrate the ease with which the calibrated PF-SPH model can be used to calculate the shape of a sessile droplet on a geometrically patterned surface. To do this, we will follow the experimental set-up of Dupuis & Yeomans (2005) in simulating a 3 μl droplet on a surface featuring square pillars, as shown in figure 12. The parameters used in these simulations are given in table 3.

Figure 13 shows a comparison between two almost identical numerical experiments – the only difference being the initial kinetic energy of the droplet before ‘impact’ with the surface. Figure 13(a) shows a settled droplet that was initialised with zero velocity. This droplet sits atop the pillars on the substrate, without enough energy to infiltrate the gaps between them. The droplet in figure 13(b) was initialised with a velocity in the vertical direction of -0.1 m s^{-1} , allowing it to overcome the energy barrier discussed by Dupuis & Yeomans (2005) and transition from a ‘suspended’ to a ‘collapsed’ state, in which the fluid has infiltrated between the pillars. That the present model reproduces this qualitative behaviour suggests it should be applicable to problems with complex surfaces.

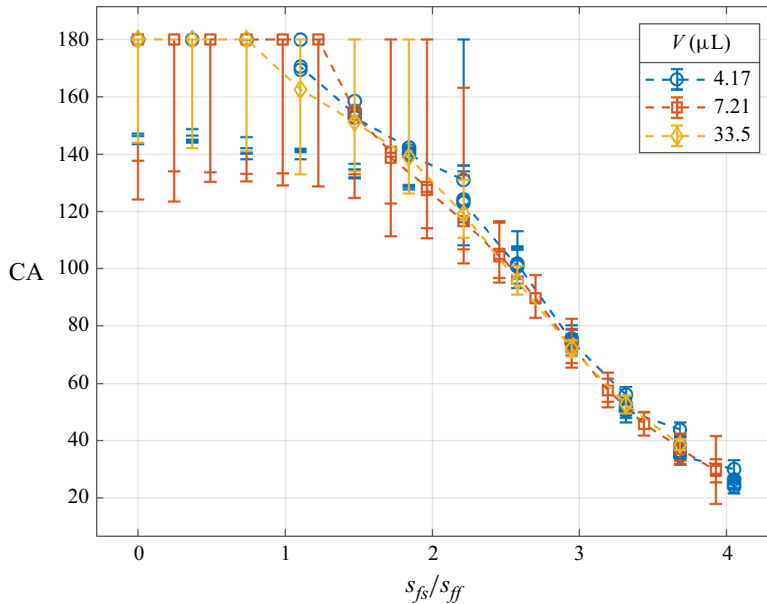


Figure 11. Contact angles, measured by fitting Y–L profiles to sessile droplet density isosurfaces, are plotted against the ratio of pairwise-force strengths, s_{fs}/s_{ff} , and grouped by volume. A droplet is excluded if the volume enclosed by the density isosurface differs from the actual droplet's volume by more than 10 %.

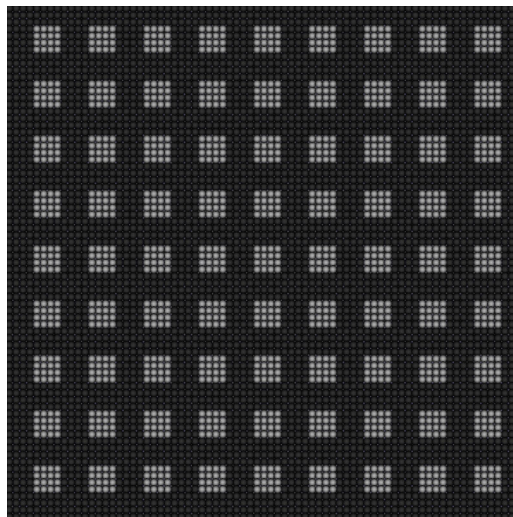


Figure 12. A top-down view of the pillared substrate used for the simulation in figure 13. The square pillars (shown in light grey) are $150\text{ }\mu\text{m}$ tall, $120\text{ }\mu\text{m}$ wide and located at regular intervals of $240\text{ }\mu\text{m}$ across the substrate (dark grey).

4.2. Chemically patterned surface

Another type of surface heterogeneity that is widely studied is a chemically patterned surface. By manufacturing a surface with, for example, alternating hydrophobic and hydrophilic stripes, one can influence the shape or motion of a droplet. Varagnolo *et al.* (2014) note that controlling the motion of very small droplets in this way is one of the

Property	Value(s)
Density, ρ_0	1000 kg m ⁻³
Viscosity, μ	0.89 mPa · s
Speed of sound, c_0	80 m s ⁻¹
Volume, V	3.0 μ l
s_{ff}	2 mN m ⁻¹
s_{fs}	4.9 mN m ⁻¹
Resolution, H	1.2×10^{-4} m
No. of particles	113 000 fluid particles

Table 3. Fluid properties in pillared substrate simulation in [figure 13](#).

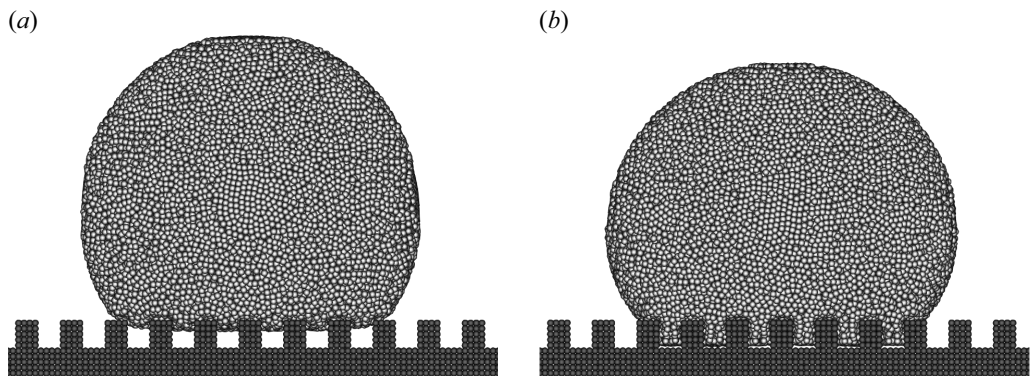


Figure 13. A comparison of nearly identical simulations of a droplet settling on the physically patterned surface of square pillars depicted in [figure 12](#). The addition of a small impact velocity changes the wetting behaviour significantly (note that these are side views of three-dimensional simulations). (a) After 10 ms of zero gravity, then 30 ms under 1 g, this droplet has settled, suspended atop the pillars, (b) 30 ms after a 0.1 m s⁻¹ impact, this droplet has infiltrated the pillars.

key problems in the design of reliable microfluidic devices. We will demonstrate that our PF-SPH is also a suitable model for the shape of a droplet settled on such a patterned surface. To include the variable wettability in the PF-SPH model, we simply modify the adhesive force strength s_{fs} across the surface, depending on whether a boundary particle is hydrophobic (low wettability, high θ_{CA}) or hydrophilic (high wettability, low θ_{CA}). The fluid properties for this simulation are given in [table 4](#). For the hydrophobic surface type, we used $s_{fs}/s_{ff} = 1.4$ for an equilibrium contact angle of $\theta_{hydrophobic} \approx 155^\circ$, and for the hydrophilic surface type, $s_{fs}/s_{ff} = 3.5$ for $\theta_{hydrophilic} \approx 45^\circ$.

One of the advantages of our PF-SPH scheme is that the relationship between the contact angle and the position and motion of the contact line is not explicitly prescribed; instead, the simulated contact angle is ultimately a function of the adhesive force strength s_{fs}/s_{ff} and the geometry of the substrate. Thus, we may use the model to study the transition between contact angles on the hydrophobic and hydrophilic zones. To visualise the contact angle on the contact line, we use the surface normal of the density isosurface (3.6) at a distance of $H/2$ above the substrate. [Figure 14](#) shows side views of the droplet and the preferential spreading on the hydrophilic stripe. The contact line is shown, coloured by the contact angle, with smooth transitions between the contact angles $\theta_{hydrophobic}$ and $\theta_{hydrophilic}$. The side views reveal that the contact angle the droplet makes is vastly different on the hydrophilic substrate sections as compared with the hydrophobic sections.

Property	Value(s)
Density, ρ_0	1261 kg m^{-3}
Viscosity, μ	$5.9 \text{ mPa} \cdot \text{s}$
Speed of sound, c_0	80 m s^{-1}
Volume, V	$0.165 \mu\text{l}$
s_{ff}	2 mN m^{-1}
s_{fs}	$7 \text{ (hydrophilic)}, 2.8 \text{ (hydrophobic) mN m}^{-1}$
Resolution, H	$4 \times 10^{-5} \text{ m}$
No. of particles	$164\,968 \text{ fluid particles}$

Table 4. Fluid properties in patterned substrate simulation in [figure 14](#).

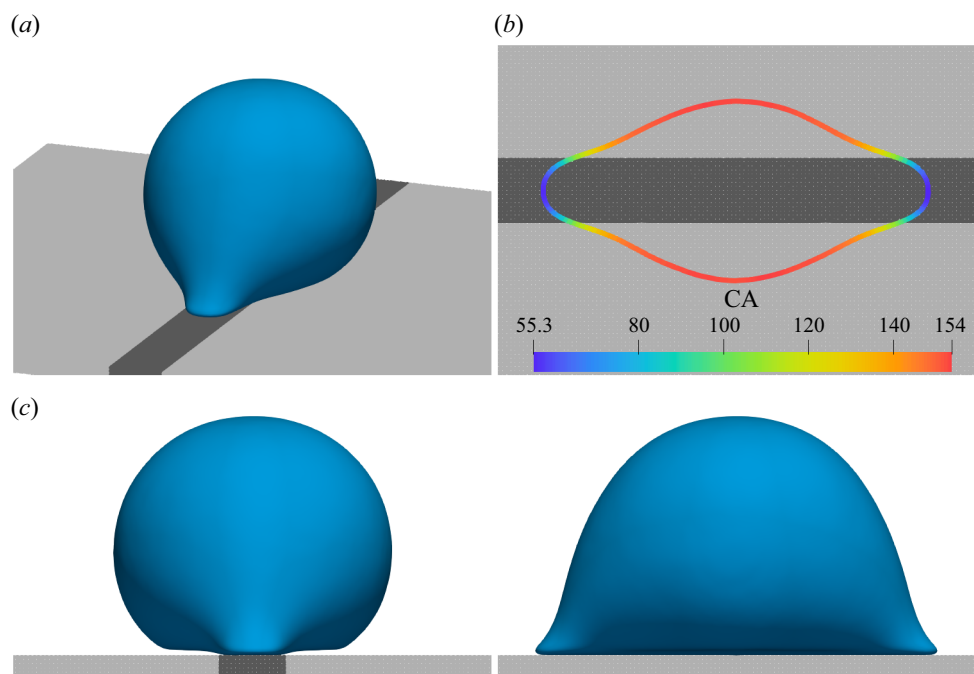


Figure 14. A droplet settles on a flat hydrophobic surface ($\theta_{CA} \approx 155^\circ$) with a hydrophilic stripe ($\theta_{CA} \approx 45^\circ$). (a) isometric view. (b) the contact angle is plotted around the contact line, showing a transition from one equilibrium contact angle to another. (c) side views of the droplet, showing the significant difference in apparent contact angles on the different surface types. Surface representations of the droplet are obtained from the density isosurface; (3.6).

At its extremities, the measured contact angle reaches the specified hydrophobic value of 155° , whereas the specified hydrophilic contact angle of 45° is not realised in the simulation, with the lowest measured contact angle being 55° . That our model is capable of producing such behaviour suggests it could be used to design and study manufactured, variable-wettability substrates for droplet motion control.

4.3. Wheat leaf

The broader context and motivation of this work is to enable the study of droplets impacting and settling on plant leaves, for which a key challenge is calculating the shape

Property	Value(s)
Density, ρ_0	1000 kg m ⁻³
Viscosity, μ	0.89 mPa · s
Speed of sound, c_0	100 m s ⁻¹
Volume, V	0.27 μ l
s_{ff}	2 mN m ⁻¹
s_{fs}	5.6 (leaf), 7.875 (hairs) mN m ⁻¹
Resolution, H	4×10^{-5} m
No. of particles	267 731 fluid particles

Table 5. Fluid properties in wheat leaf simulation in [figure 15](#).

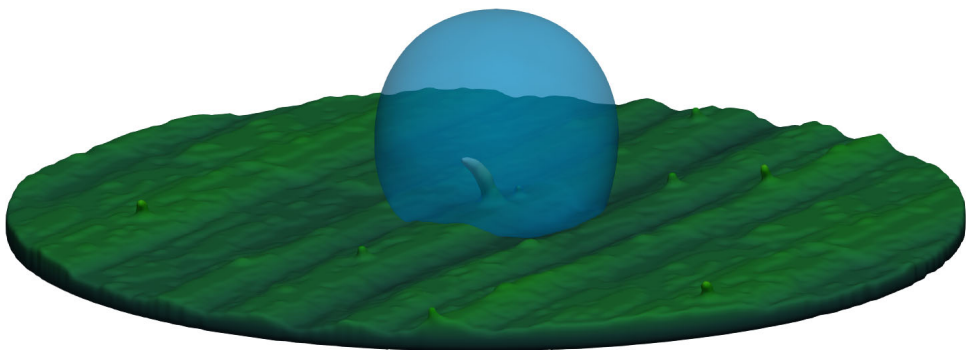


Figure 15. A PF-SPH simulation of a 0.27 μ L water droplet settled on the surface of a wheat leaf after 12 ms. The droplet's liquid–gas interface is rendered by polygonising an isosurface of the density field, $\langle \rho(\mathbf{x}) \rangle = \rho_0/2$. The leaf surface is rendered similarly, using only boundary particles, and coloured by height for clarity. A hair on the leaf surface is visible under the translucent droplet.

of a droplet on a plant leaf with microscopic roughness, and chemical heterogeneity (Mayo *et al.* 2015). Here, we will demonstrate the model's applicability to complex surfaces – specifically, a reconstructed wheat leaf surface. This virtual wheat leaf was reconstructed from a micro computed tomography scan using a radial basis function partition of unity method as described in related work: Whebell *et al.* (2025). We discretise this surface for an SPH simulation by taking a block of boundary particles on a regular grid, and discarding any for which the implicit surface indicator function is negative ($\mathcal{F}(\mathbf{x}) < 0$). Manually selected boundary particles are labelled as hairs and assigned a higher adhesive force strength to reflect the surface chemistry of real wheat leaves. The parameters for this simulation are given in [table 5](#).

We initialised the simulation with a sphere of fluid particles just above a hair of the wheat leaf, with zero impact velocity, to study how the droplet settles onto the surface. [Figure 15](#) shows the shape of the droplet at 50 ms, once it has lost momentum and settled on the leaf. We can visualise the contact line with a contour line on the density isosurface, where the approximate minimum distance to the leaf surface is $2\Delta x$. Specifically, [figure 16](#) shows the contact line visualised as the set of points

$$\left\{ \mathbf{x} : \sum_{j \in \mathcal{I}_f} m_j W(\mathbf{x} - \mathbf{x}_j; H) = \frac{\rho_0}{2} \right\} \cap \left\{ \mathbf{x} : \min_{\mathbf{y} \in \mathcal{L}} \|\mathbf{x} - \mathbf{y}\| = 2\Delta x \right\}, \quad (4.1)$$

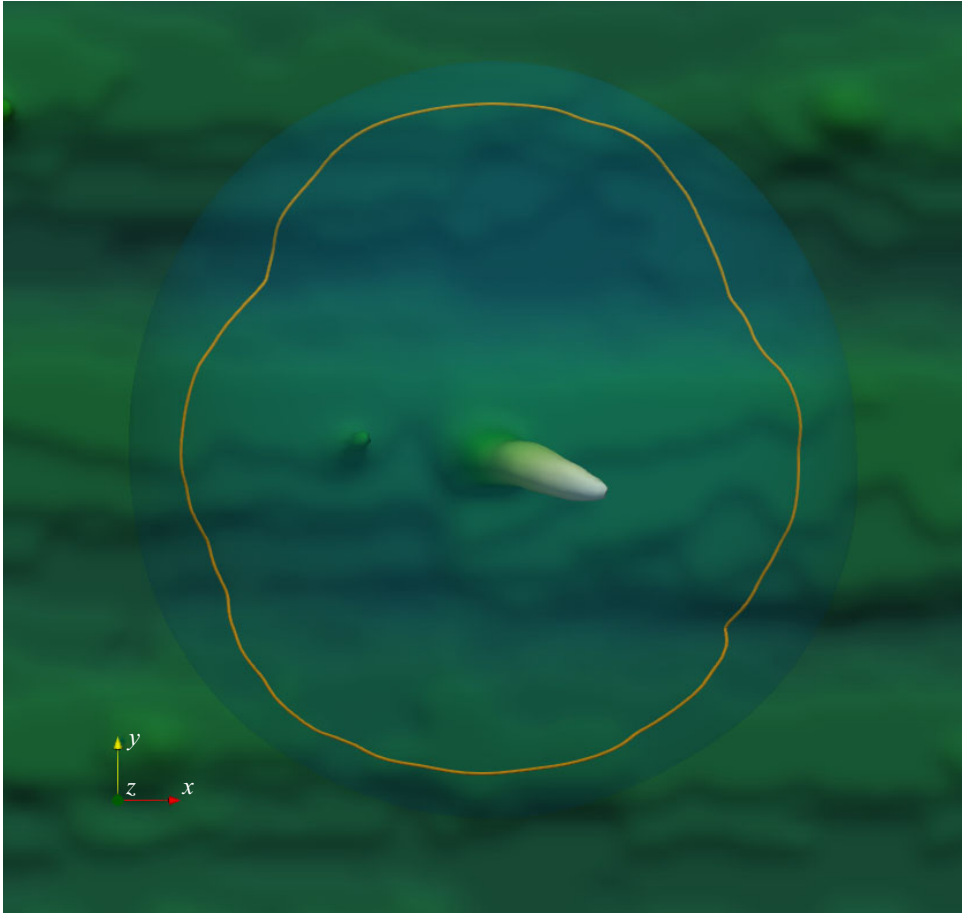


Figure 16. The contact line of the droplet on a wheat leaf depicted in [figure 15](#), visualised by computing the set of points on the density isosurface that are $2\Delta x$ from the surface.

where \mathcal{L} is the set of leaf surface points. Note the highly irregular contact line following the natural curvature of the wheat leaf. This droplet shape could be used to measure the wetted area of the leaf surface or serve as an initial condition for an evaporation model in future work.

4.4. Discussion on pairwise-force profiles

The exact design of the pairwise-force profile f_{ij} is in need of more investigation before the PF-SPH model can be applied as readily as, for example, the CSF formulation. Literature on the effect of the force profile is scarce. Tartakovsky & Panchenko (2016) report some analytical results predicting the surface tension from $f_{ij}(\tau)$ and s_{ij} in multiphase simulations, but we could not verify these results in our single phase simulations. Our force profile causes most fluid–fluid particle interactions to be attractive, which could cause excess numerical stress in the fluid. In the simulations tested, the mostly attractive pairwise force has the somewhat desirable effect of keeping the particle distribution ordered – for example, in a high velocity impact event – which ensures that interpolation error is low. More investigation is needed to quantify the dissipative effect of the pairwise forces before this model is applied to viscosity-dependent scenarios.

5. Conclusion

We have presented a weakly compressible PF-SPH model and applied it to study droplet shapes on complex surfaces. A new physically motivated pairwise-force profile $f_{ij}(\tau)$ has been validated and calibrated to relate cohesive and adhesive parameters s_{ff} and s_{fs} to physical values of the surface tension and contact angle. Furthermore, we have described a method for calibrating the contact angle of PF-SPH models and shown that the liquid–gas interfaces of simulated droplets on flat surfaces are in good agreement with semi-analytical solutions to the Young–Laplace equations for a range of contact angles between 40° and 180° . The pairwise-force model is scale-independent and, since it does not rely on resolving interfaces, robust to complex surface morphology.

The test cases we present in §4 demonstrate that this method should be applicable to a broad range of droplet-related problems on substrates of interest, at least for sessile droplets and low-inertial flows. In future work, we intend to model the chemical heterogeneity of plant leaf surfaces by varying the adhesive parameter s_{fs} across the surface to more accurately reflect the real surface chemistry. Other potential applications include the study of spreading and impaction on rough or patterned surfaces. With the careful parameter calibration developed here, the pairwise-force model shows promise for simulating droplets on otherwise challenging substrates.

Acknowledgements. We thank the associated industry partners Syngenta, NuFarm and Plant Protection Chemistry NZ for their involvement, and collaborators J. Cooper-White and P. Taylor for many fruitful discussions. Computational resources used in this work were provided by the eResearch Office, Queensland University of Technology, Brisbane, Australia.

Funding. This work was financially supported by an Australian Research Council Research Training Program scholarship, as well as the Australian Research Council Linkage Grant LP160100707 and associated industry partners Syngenta and Nufarm.

Declaration of interests. The authors report no conflict of interest.

REFERENCES

- ALLEN, M.P. & TILDESLEY, D.J. 1989 *Computer Simulation of Liquids*, corrected edn. Clarendon Press.
- ANTUONO, M., MARRONE, S. & COLAGROSSI, A. 2025 Coalescing and break-up of viscous drops with surface tension through the smoothed particle hydrodynamics. *Comput. Method. Appl. Mech. Engng* **442**, 118014.
- ARAI, E., TARTAKOVSKY, A., HOLT, R.G., GRACE, S. & RYAN, E. 2020 Comparison of surface tension generation methods in smoothed particle hydrodynamics for dynamic systems. *Comput. Fluids* **203**, 104540.
- BARREIRO, A., CRESPO, A., DOMÍNGUEZ, J. & GÓMEZ-GESTEIRA, M. 2013 Smoothed particle hydrodynamics for coastal engineering problems. *Comput. Struct.* **120**, 96–106.
- BLANK, M., NAIR, P. & PÖSCHEL, T. 2024 Surface tension and wetting at free surfaces in smoothed particle hydrodynamics. *J. Fluid Mech.* **987**, A23.
- BONET, J. & LOK, T.-S. 1999 Variational and momentum preservation aspects of smooth particle hydrodynamic formulations. *Comput. Method. Appl. Mech. Engng* **180**, 97–115.
- BORMASHENKO, E.Y. 2017 *Physics of Wetting: Phenomena and Applications of Fluids On Surfaces*. De Gruyter.
- BRACKBILL, J., KOTHE, D. & ZEMACH, C. 1992 A continuum method for modeling surface tension. *J. Comput. Phys.* **100**, 335–354.
- BROWN, R., ORR, F. & SCRIVEN, L. 1980 Static drop on an inclined plate: analysis by the finite element method. *J. Colloid Interface Sci.* **73**, 76–87.
- CHAMAKOS, N.T., SEMA, D.G. & PAPATHANASIOU, A.G. 2021 Progress in modeling wetting phenomena on structured substrates. *Arch. Comput. Method. Engng* **28**, 1647–1666.
- CHIRON, L., DE LEFFE, M., OGER, G. & LE TOUZÉ, D. 2019 Fast and accurate SPH modelling of 3D complex wall boundaries in viscous and non viscous flows. *Comput. Phys. Commun.* **234**, 93–111.
- COLAGROSSI, A., ANTUONO, M. & LE TOUZÉ, D. 2009 Theoretical considerations on the free-surface role in the smoothed-particle-hydrodynamics model. *Phys. Rev. E* **79**, 056701.

- COLE, R.H. 1948 *Underwater Explosions*. Princeton University Press.
- CRESPO, A., DOMÍNGUEZ, J., ROGERS, B., GÓMEZ-GESTEIRA, M., LONGSHAW, S., CANELAS, R., VACONDIO, R., BARREIRO, A. & GARCÍA-FEAL, O. 2015 DualSPHysics: Open-source parallel CFD solver based on Smoothed Particle Hydrodynamics (SPH). *Comput. Phys. Commun.* **187**, 204–216.
- CRESPO, A.C., DOMINGUEZ, J.M., BARREIRO, A., GÓMEZ-GESTEIRA, M. & ROGERS, B.D. 2011 GPUs, a new tool of acceleration in CFD: efficiency and reliability on smoothed particle hydrodynamics methods. *PLoS ONE* **6**, e20685.
- DANOV, K.D., DIMOVA, S.N., IVANOV, T.B. & NOVEV, J.K. 2016 Shape analysis of a rotating axisymmetric drop in gravitational field: comparison of numerical schemes for real-time data processing. *Colloids Surf. A: Physicochem. Engng Aspects* **489**, 75–85.
- DEHNEN, W. & ALY, H. 2012 Improving convergence in smoothed particle hydrodynamics simulations without pairing instability: SPH without pairing instability. *Mon. Not. R. Astron. Soc.* **425**, 1068–1082.
- DOMÍNGUEZ, J.M., CRESPO, A.J.C., GÓMEZ-GESTEIRA, M. & MARONGIU, J.C. 2011 Neighbour lists in smoothed particle hydrodynamics. *Intl J. Numer. Meth. Fluids* **67**, 2026–2042.
- DOMÍNGUEZ, J.M., *et al.* 2022 DualSPHysics: from fluid dynamics to multiphysics problems. *Comput. Part. Mech.* **9**, 867–895.
- DORR, G.J., FORSTER, W.A., MAYO, L.C., MCCUE, S.W., KEMPTHORNE, D.M., HANAN, J., TURNER, I.W., BELWARD, J.A., YOUNG, J. & ZABKIEWICZ, J.A. 2016 Spray retention on whole plants: modelling, simulations and experiments. *Crop Protection* **88**, 118–130.
- DORR, G.J., WANG, S., MAYO, L.C., MCCUE, S.W., FORSTER, W.A., HANAN, J. & HE, X. 2015 Impaction of spray droplets on leaves: influence of formulation and leaf character on shatter, bounce and adhesion. *Exp. Fluids* **56**, 143.
- DUPUIS, A. & YEOMANS, J.M. 2005 Modeling droplets on superhydrophobic surfaces: equilibrium states and transitions. *Langmuir* **21**, 2624–2629.
- GINGOLD, R.A. & MONAGHAN, J.J. 1977 Smoothed particle hydrodynamics: theory and application to non-spherical stars. *Mon. Not. R. Astron. Soc.* **181**, 375–389.
- HARTLAND, S. & HARTLEY, R.W. 1976 *Axisymmetric Fluid-Liquid Interfaces: Tables Giving the Shape of Sessile and Pendant Drops and External Menisci, with Examples of Their Use*. Elsevier Scientific Pub. Co.
- HOCKING, L.M. 1992 Rival contact-angle models and the spreading of drops. *J. Fluid Mech.* **239**, 671–681.
- HOOVER, W.G. 1998 Isomorphism linking smooth particles and embedded atoms. *Physica A: Stat. Mech. Applics.* **260**, 244–254.
- IHMSEN, M., AKINCI, N., BECKER, M. & TESCHNER, M. 2011 A parallel SPH implementation on multi-core CPUs. *Comput. Graph. Forum* **30**, 99–112.
- JAMALI, M. & TAFRESHI, H.V. 2021 Numerical simulation of two-phase droplets on a curved surface using surface evolver. *Colloids Surf. A: Physicochem. Engng Aspects* **629**, 127418.
- JANSEN, H.P., BLIZNYUK, O., KOOIJ, E.S., POELSEMA, B. & ZANDVLIET, H.J.W. 2012 Simulating anisotropic droplet shapes on chemically striped patterned surfaces. *Langmuir* **28**, 499–505.
- JONES, J.E. 1924 On the determination of molecular fields.—I. From the variation of the viscosity of a gas with temperature. *Proc. R. Soc. Lond. A* **106**, 441–462.
- KORDILLA, J., TARTAKOVSKY, A.M. & GEYER, T. 2013 A smoothed particle hydrodynamics model for droplet and film flow on smooth and rough fracture surfaces. *Adv. Water Resour.* **59**, 1–14.
- LANDAU, L.D. & LIFSHITZ, E.M. 1987 Fluid mechanics. In *Course of Theoretical Physics*, 2nd edn, vol. 6. Pergamon Press.
- LEIMKUHLER, B. & MATTHEWS, C. 2015 Molecular dynamics: with deterministic and stochastic numerical methods. In *Interdisciplinary Applied Mathematics*, vol. 39. Springer International Publishing.
- LIU, M., MEAKIN, P. & HUANG, H. 2006 Dissipative particle dynamics with attractive and repulsive particle-particle interactions. *Phys. Fluids* **18**, 017101.
- LUCY, L.B. 1977 A numerical approach to the testing of the fission hypothesis. *Astron. J.* **82**, 1013.
- MACIA, F., ANTUONO, M., GONZALEZ, L.M. & COLAGROSSI, A. 2011 Theoretical analysis of the no-slip boundary condition enforcement in SPH methods. *Prog. Theor. Phys.* **125**, 1091–1121.
- MAYO, L.C., MCCUE, S.W., MORONEY, T.J., FORSTER, W.A., KEMPTHORNE, D.M., BELWARD, J.A. & TURNER, I.W. 2015 Simulating droplet motion on virtual leaf surfaces. *R. Soc. Open Sci.* **2**, 140528.
- MONAGHAN, J.J. 1994 Simulating free surface flows with SPH. *J. Comput. Phys.* **110**, 399–406.
- MONAGHAN, J.J. 2005 Smoothed particle hydrodynamics. *Rep. Prog. Phys.* **68**, 1703–1759.
- MONAGHAN, J.J. & GINGOLD, R. 1983 Shock simulation by the particle method SPH. *J. Comput. Phys.* **52**, 374–389.
- MORRIS, J.P. 2000 Simulating surface tension with smoothed particle hydrodynamics. *Intl J. Numer. Meth. Fluids* **33**, 333–353.

- MÜLLER, M., SCHIRM, S. & TESCHNER, M. 2004 Interactive blood simulation for virtual surgery based on smoothed particle hydrodynamics. *Technol. Health Care* **12**, 25–31.
- NAIR, P. & PÖSCHEL, T. 2018 Dynamic capillary phenomena using incompressible SPH. *Chem. Engng Sci.* **176**, 192–204.
- RAVI ANNAPRAGADA, S., MURTHY, J.Y. & GARIMELLA, S.V. 2012 Droplet retention on an incline. *Intl J. Heat Mass Transfer* **55**, 1457–1465.
- RAYLEIGH, L. 1879 VI. On the capillary phenomena of jets. *Proc. R. Soc. Lond. A* **29**, 71–97.
- SANTACRUZ-YUNGA, E., GUERRERO-RODRÍGUEZ, B., SILVA-ROJAS, P., PÉREZ-ROA, R., SIGALOTTI, L.D.G., TREJO, C. & PLAZA, E. 2025 A pair potential force model for surface tension calculations with smoothed particle hydrodynamics. *Comput. Part. Mech.* Available at: <https://link.springer.com/article/10.1007/s40571-025-00948-7>.
- SHIGORINA, E., KORDILLA, J. & TARTAKOVSKY, A.M. 2017 Smoothed particle hydrodynamics study of the roughness effect on contact angle and droplet flow. *Phys. Rev. E* **96**, 033115.
- SPRINGEL, V. 2010 Smoothed particle hydrodynamics in astrophysics. *Annu. Rev. Astron. Astrophys.* **48**, 391–430.
- TARTAKOVSKY, A. & MEAKIN, P. 2005 Modeling of surface tension and contact angles with smoothed particle hydrodynamics. *Phys. Rev. E* **72**, 026301.
- TARTAKOVSKY, A. & PANCHENKO, A. 2016 Pairwise force smoothed particle hydrodynamics model for multiphase flow: surface tension and contact line dynamics. *J. Comput. Phys.* **305**, 1119–1146.
- TREDENICK, E.C., FORSTER, W.A., PETHIYAGODA, R., VAN LEEUWEN, R.M. & MCCUE, S.W. 2021 Evaporating droplets on inclined plant leaves and synthetic surfaces: experiments and mathematical models. *J. Colloid Interface Sci.* **592**, 329–341.
- VARAGNOLO, S., SCHIOCCHET, V., FERRARO, D., PIERNO, M., MISTURA, G., SBRAGAGLIA, M., GUPTA, A. & AMATI, G. 2014 Tuning drop motion by chemical patterning of surfaces. *Langmuir* **30**, 2401–2409.
- VERGNAUD, A., OGER, G., LE TOUZÉ, D., DELEFFE, M. & CHIRON, L. 2022 C-CSF: accurate, robust and efficient surface tension and contact angle models for single-phase flows using SPH. *Comput. Method. Appl. Mech. Engng* **389**, 114292.
- WANG, Z.-B., CHEN, R., WANG, H., LIAO, Q., ZHU, X. & LI, S.-Z. 2016 An overview of smoothed particle hydrodynamics for simulating multiphase flow. *Appl. Math. Model.* **40**, 9625–9655.
- WENDLAND, H. 1995 Piecewise polynomial, positive definite and compactly supported radial functions of minimal degree. *Adv. Comput. Maths* **4**, 389–396.
- WHEBELL, R.M., MORONEY, T.J., TURNER, I.W., PETHIYAGODA, R., WILLE, M.-L., COOPER-WHITE, J.J., KUMAR, A., TAYLOR, P. & MCCUE, S.W. 2025 Data fusion for a multiscale model of a wheat leaf surface: a unifying approach using a radial basis function partition of unity method. *SIAM J. Imaging Sci.* **18**, 1417–1438.
- YE, T., PAN, D., HUANG, C. & LIU, M. 2019 Smoothed particle hydrodynamics (SPH) for complex fluid flows: recent developments in methodology and applications. *Phys. Fluids* **31**, 011301.
- ZHU, Y. & FOX, P.J. 2001 Smoothed particle hydrodynamics model for diffusion through porous media. *Trans. Porous Med.* **43**, 441–471.